

This manuscript has been authored by UT-Battelle, LLC under Contract No. DE-AC05-00OR22725 with the U.S. Department of Energy. The United States Government retains and the publisher, by accepting the article for publication, acknowledges that the United States Government retains a non-exclusive, paid-up, irrevocable, world-wide license to publish or reproduce the published form of this manuscript, or allow others to do so, for United States Government purposes. The Department of Energy will provide public access to these results of federally sponsored research in accordance with the DOE Public Access Plan (<http://energy.gov/downloads/doe-public-access-plan>)

Competitive and Cooperative electronic states in $\text{Ba}(\text{Fe}_{1-x}\text{T}_x)_2\text{As}_2$

with $\text{T}=\text{Co, Ni, Cr}$

Qiang Zou¹, Mingming Fu^{1,2}, Zhiming Wu², Li Li³, David S. Parker³, Athena S. Sefat³, and Zheng Gai^{1,*}

¹Center for Nanophase Materials Sciences, Oak Ridge National Laboratory, Oak Ridge, TN 37831, USA

²Fujian Provincial Key Laboratory of Semiconductors and Applications, Collaborative Innovation Center for Optoelectronic Semiconductors and Efficient Devices, Department of Physics, Xiamen University, Xiamen, Fujian Province, 361005, P. R. China

³Materials Science & Technology Division, Oak Ridge National Laboratory, Oak Ridge, TN 37831, USA

* Corresponding author: gaiz@ornl.gov

Abstract

The electronic structure inhomogeneities in Co, Ni, and Cr doped BaFe_2As_2 ‘122’ single crystals are compared using scanning tunneling microscopy/spectroscopy (STM/S) at nanoscales within three different global property regions: pure superconducting (SC) dome (Co-122), coexisting of SC and antiferromagnetic (AFM) region (Ni-122), and non-SC region (Cr-122). Machine learning method is utilized to categorize the various nanometer-size inhomogeneous electronic states described here as in-gap, L-shape and S-shape states immersed into the SC matrix for Ni-and Co-doped 122, and L-shape and S-shape states into metallic matrix for Cr-doped 122. Although the relative percentages of in-gap, L-shape and S-shape states vary in the three samples, the total volume fraction of the three electronic states are quite similar, coincident with the electron

(Ni_{0.04} and Co_{0.08}) and hole (Cr_{0.04}) numbers doped into the 122 compound. By combining the volume fractions of the three states, local density of the states (LDOS), field dependent behavior and global properties in these three sets of samples, the in-gap state is confirmed as a magnetic impurity state from the Co or Ni dopants, the L-shape state is identified as a spin density wave (SDW) which competes with the SC phase, and the S-shape state is found to be another form of magnetic order which constructively cooperates with the SC phase rather than competing with it. The comparison of the vortex structures indicates that those inhomogeneous electronic states serve as pinning centers for stabilizing the hexagonal vortex lattice.

Keywords: Iron-based superconductor, magnetic dopant, scanning tunneling microscopy / spectroscopy, electronic inhomogeneity, spin density wave

Introduction

The interplay between magnetism and superconductivity (SC) is still one of the fundamental issues in understanding the mechanism of superconductivity of unconventional superconductors, like cuprates and iron-based superconductor (FeSC) ¹⁻², for the reason that SC in these materials always appears near antiferromagnetic (AF) order. In cuprates, experiments demonstrated that the superconducting pairing state is dx^2-y^2 , which is induced by spin fluctuations ³⁻⁵. Similar to cuprates, magnetism in FeSC is also believed to play an important role in the electron pairing mechanism ^{2,4}. However, in FeSC, it is more complicated thus more controversial because five Fe 3d orbitals form multiple Fermi surfaces (FS), while in cuprates only single Cu d-band crosses the FS ⁶⁻⁹. As one of the results of the complexity, in the most studied FeSC family Iron pnictides BaFe₂As₂ (122), SC can be realized by atomic substitution at any element site, for

example by hole-doping onto Ba site¹⁰, electron-doping on Fe site^{11 12} and isovalent doping to As site¹³. However, it is found the crystals with electron-doping to Fe site with Ni and Co are superconducting while hole-dopant Cr-122 crystals are not¹⁴.

On the other hand, for the electron-doping 122 crystals, it is well established that upon electron doping via Co/Ni substitution for Fe, the collinear long-range AF order is suppressed, and SC appears. However, there is ongoing debates concerning the relationship between the AF order and SC. One perspective is the itinerant nature of magnetism: the static AF order arises from the formation of a spin-density-wave induced by itinerant electrons and Fermi surface nesting of the electron and hole pockets, upon doping the pair scattering between the electron and hole like FS pockets leads to SC¹⁵⁻¹⁶. A different perspective is the localized nature of magnetism: the short-range incommensurate AF order is the cluster spin glass phase as a consequence of the disordered localized moments^{12, 17}. There is also a perspective that local moments and itinerant electrons coexist, in which part of the Fe d bands are delocalized and contribute to the itinerancy, whereas the others are localized due to strong correlation effect and provide the source for local moments¹⁸⁻¹⁹. This model was used to explain the scanning tunneling microscopic observation of the coexistence as well as co-disappearance of pseudogap-like feature and superconductor in NaFe_{1-x}Co_xAs (Co-111) system where the pure itinerant picture fails²⁰. A muon spin rotation study also observed a spatially inhomogeneous magnetic state develops below T_c which has a constructive relationship with SC in near optimal or overdoped Co-122 samples²¹⁻²². This is intrinsically different from the reported SDW phase in NaFe_{1-x}Co_xAs (Co-111) which is competitively anti-correlate with the SC phase²³.

Here, we investigate the local electronic structure of 122 crystalline matrix BaFe₂As₂ that is doped with magnetic elements (Ni, Co, or Cr) at the same amount of electron versus hole doping

levels per Fe atom, and systematically explore the electronic structure signatures of the magnetism and SC phases using low temperature high magnetic-field scanning tunneling microscopy/spectroscopy (STM/S). The machine learning technique of K-means clustering method is utilized to categorize the various nanometer-size inhomogeneous electronic states. Other than the SC state, in-gap state, competitive L-shape and cooperative S-shape states are found to coexist in the samples. The in-gap state in SC crystals is confirmed as a magnetic impurity state from Co or Ni dopants; the L-shape state is identified as SDW which competes with the SC phase; the S-shape state originated from local magnetic order which constructively cooperates with the SC phase rather than competing with it. The comparison of the vortex structures indicates that those inhomogeneous electronic states serve as pinning centers for stabilizing the hexagonal vortex lattice for the bulk superconductors.

Results

For the purpose of comparison, three sets of samples of the transition metal substituted $\text{Ba}(\text{Fe}_{1-x}\text{T}_x)_2\text{As}_2$ in three different bulk property regions (bulk SC, magnetism and SC coexistence, non-SC) are studied, including the AFM phase in $\text{Ba}(\text{Fe}_{0.96}\text{Cr}_{0.04})_2\text{As}_2$ (Cr-122), the coexisting region with AFM and SC phase in $\text{Ba}(\text{Fe}_{0.96}\text{Ni}_{0.04})_2\text{As}_2$ (Ni-122), and the bulk SC phase in $\text{Ba}(\text{Fe}_{0.92}\text{Co}_{0.08})_2\text{As}_2$ (Co-122). Ni (Cr) doping introduces twice the number of electrons (holes) in the FeAs layer as that of Co doping from electron counting, so we select the Co-122 doping level as 0.08 instead of 0.04. These phases are indicated using blue, red and yellow balls in the temperature-composition (T-x) phase diagram in Fig. 1(a); the structure of 122 unit cell is in inset. At the temperature of experiments in this work (4 K), Cr-122 has a G-AFM ground state ($T_N \sim 100$ K); optimally doped Co-122 is in SC state ($T_c \sim 22$ K)²⁴; and the composition of the Ni-122 was picked to locate it in the coexistence range of SC and AFM orders ($T_c \sim 19$ K, $T_N \sim 45$ K).

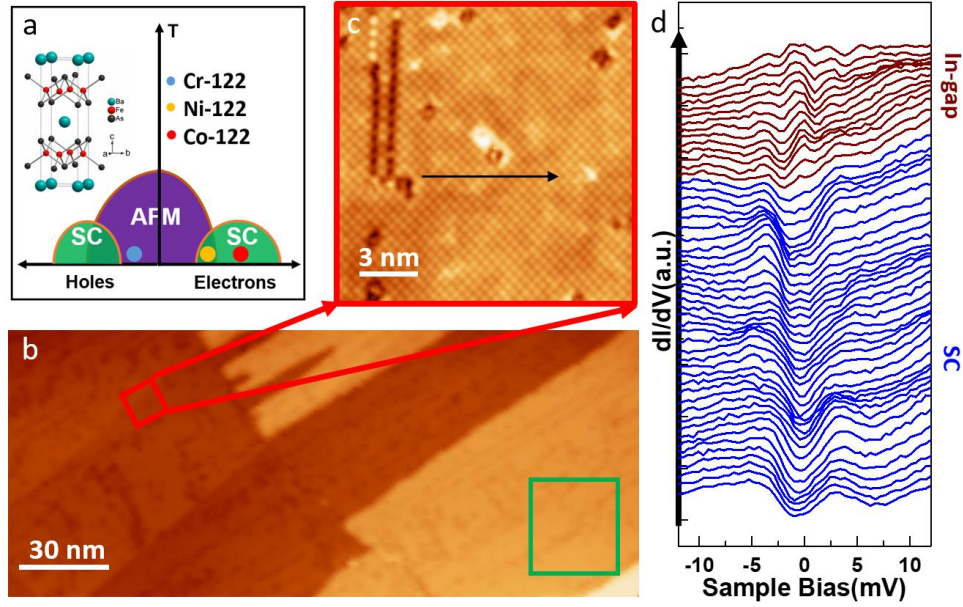


Fig. 1. | Morphology and electronic structure of $\text{Ba}(\text{Fe}_{0.96}\text{Ni}_{0.04})_2\text{As}_2$. (a) The phase diagram of BaFe_2As_2 under doping concentration variation. The inset is the crystal structure of the parent compound of BaFe_2As_2 . (b) The large scale STM topography image of Ni-122, $V_{\text{Bias}} = -20$ mV, $I_t = 100$ pA. The red and green boxes mark the locations of (c) and Fig. 2 (a), respectively. (c) Atomically resolved STM image on Ni-122 surface ($V_{\text{Bias}} = -100$ mV, $I_t = 400$ pA), shows $\sqrt{2} \times \sqrt{2}$ reconstruction. (d) Sets of STS spectra along the black arrow in (c), show local electronic inhomogeneity. The blue and brown curves show superconducting and in-gap states as labeled. Curves are shifted vertically for clarity.

After low temperature cleavage, the three sets of samples show similar topography, which is the coexistence of As terminated 2×1 and Ba terminated $\sqrt{2} \times \sqrt{2}$ reconstructions, as reported for Co-122 before²⁵. Fig. 1(b) shows a typical large-scale topographic image of Ni-122, with terraces, steps in 0.7 nm (half unit cell in c axis) and defects. The atomic resolution image collected from the red boxes of Fig. 1(b) reveal the details of the $\sqrt{2} \times \sqrt{2}$ reconstruction, atomic scale dark pits, protrusions and dark lines, as shown in Fig. 1(c). The dark lines are the antiphase boundaries of the $\sqrt{2} \times \sqrt{2}$ domains, the dark pits are the results of missing single or multiple Ba atoms on the top surface, and the bright protrusions reflect the electronic contributions of the elemental defects

beneath the Ba surface based on the height of the protrusion (~ 0.04 nm). Note that there are less than 20 pm height-variations even on atomically well-ordered areas, suggesting the existence of an electronic contribution from sub-surface alien elements (impurities or dopants).

Dramatic local electronic inhomogeneity is found on the Ni-122 surface. Fig. 1(d) presents the STS spectroscopies along the black arrow in Fig. 1(c). Although the morphology of the areas around the arrow is similar ($\sqrt{2} \times \sqrt{2}$, no defects), the STS spectra, which are proportional to the local density of states (LDOS), show totally different features. The spectra along the black arrow exhibits superconducting coherent peaks with an SC gap width of about 4.5 meV. However, the brown spectra along the arrow show an in-gap state around the Fermi level with the suppression of the SC coherent peaks.

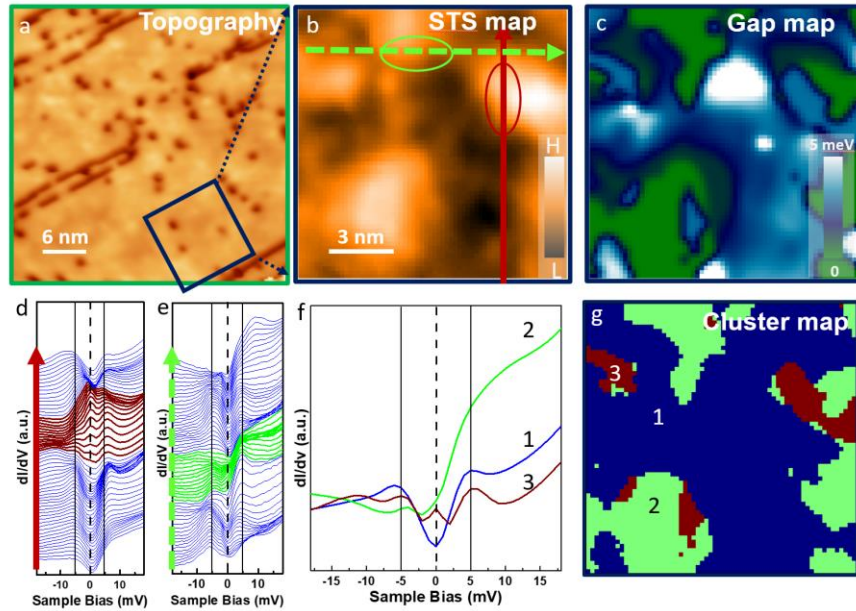


Fig. 2 | Electronic inhomogeneity on the surface of $\text{Ba}(\text{Fe}_{0.96}\text{Ni}_{0.04})_2\text{As}_2$. (a) The STM topography image of Ni-122 from the green box in Fig. 1(a), $V_{\text{Bias}} = -20$ mV and $I_t = 100$ pA. (b) STS map at Fermi level (0 meV) and (c) superconducting gap map from the same area (blue box in (a)). (d) and (e) The line STS spectra along the brown and green arrows in (b). Brown and green circles in (b) and spectra in (d) and (e) outline the non-SC areas. (f) Three K-

means principal responses and (g) cluster map which shows the spatial distribution of each type of spectroscopy from the same area as (b) and (c).

To clarify the correlation between the topography and the local electronic inhomogeneity on Ni-122, current imaging tunneling spectroscopy (CITS) maps were collected from various surfaces. Systematic comparison among topography, CITS, and SC gap map concludes that there is no apparent correlation between the topography and local electronic inhomogeneity. Such a comparison from an area with fairly ordered $\sqrt{2} \times \sqrt{2}$ reconstruction and few defects (blue box in Fig. 2(a)) is shown in Fig. 2. Shown in Fig. 2(b) and 2 (c) are the STS map at Fermi level and the corresponding gap map. Patches of non-SC areas (green) are immersed in the SC matrix (blue to white area, with various SC gap width). The nanometer size inhomogeneity in the STS map and gap map are highly correlated to each other, but not with the almost homogeneous topographic image. To reveal the intrinsic electronic structure of the inhomogeneity, an extensive survey of the spectroscopies on the surface is conducted. Other than the SC gap features, two other types of characteristic STS are found on the Ni-122 surface, also noncorrelated to the topography. Two such areas are circled in blue and brown in Fig. 2(b). Line STS in Fig. 2(d) and (e) along the dashed green and solid brown arrows in Fig. 2(b) reveal the electronic structures surrounding the inhomogeneity areas, changing gradually from SC (blue curves) to non-SC (brown or green curves). The brown curves in Fig. 2(d) show the suppression of the SC coherent peak by an in-gap state around the Fermi level, the suppression extends around 1 nm away from the center of the brown circle in Fig. 2(b), consistent with the observation of the magnetic impurity induced in-gap state in Co-122²⁵. The green curves in Fig. 2(e) have an elevated density of state at Fermi level, we name them as S-shape state in this work.

In order to analyze the spatial distribution of all three types of spectra, K-means clustering analysis of the $64 \text{ pixels} \times 64 \text{ pixels}$ spectra of CITS in Ni-122 are performed. K-means clustering is a vector quantization data mining approach, which groups a large dataset into components with quintessential characteristics²⁶. Fig. 2(f) shows the three principal responses in the data set, by comparing with Fig. 2(d) and (e), they correspond to SC, in-gap and S-shape state, respectively. The spatial distribution of the three states is shown in the cluster map in Fig. 2(g). As expected, SC state of the K-means clusters distribute at the same areas as the STS map and gap map in Fig. 2(b) and (c). Furthermore, the non-SC areas are clearly categorized into areas of in-gap state (brown) and S-shape state (green).

The above coexistence of S-shape and in-gap states with superconducting states are not affected by the surface termination; they are also observed on 2×1 surfaces. A STM study of BaFe_2As_2 has found both $\sqrt{2} \times \sqrt{2}$ and 2×1 surface reconstruction coexistence on the cleavage surface^{25,27}. As reported recently, although different terminations with different LDOS coexist on the surface of the transition metal substituted BaFe_2As_2 ($\sqrt{2} \times \sqrt{2}$ and 2×1), the superconductivity gap width is not affected by the surface reconstructions owing to the global nature of the superconductivity²⁵. These observations suggest that the S-shape, in-gap states and superconducting states are the intrinsic electronic structure of superconducting 122 system rather than the surface specific properties.

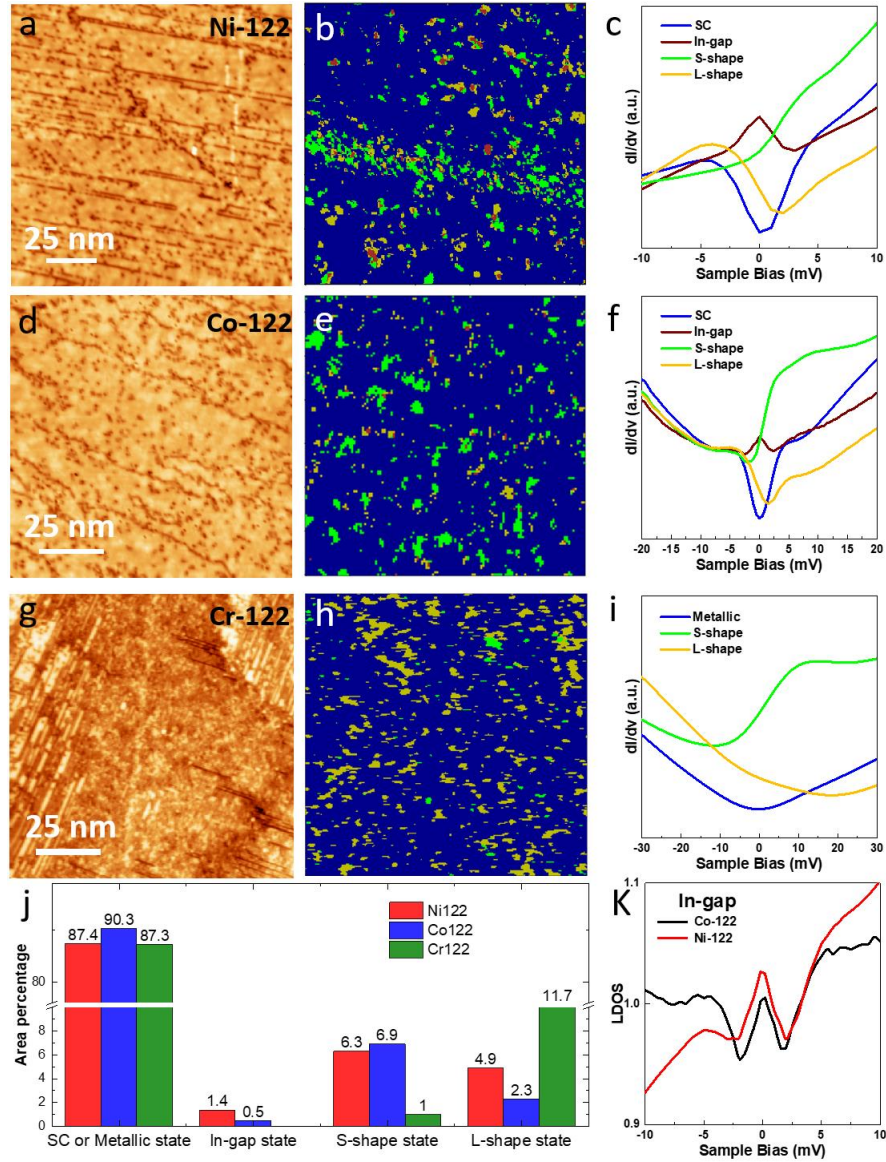


Fig. 3 | K-means clustering comparison of Ni-122, Co-122 and Cr-122. STM topographies of Ni-122 (a), Co-122 (d) and Cr-122 (g). (b), (e) and (h) Cluster maps constructed from CITS simultaneously collected with (a), (d) and (g). (c), (f) and (i) K-means principal responses of (b), (e) and (h). (j) The statistics of the area percentages of the principal responses in Ni-122, Co-122 and Cr-122. (k) LDOS comparison of the in-gap state of Ni-122 and Co-122.

The successful grouping of the characteristic states from large dataset of CITS in Ni-122 provides the K-means clustering analysis a convenient tool for a statistical comparison of the

transition metal substituted $\text{Ba}(\text{Fe}_{1-x}\text{T}_x)_2\text{As}_2$, i.e., Ni-122, Co-122 and Cr-122; shown in Fig. 3(a), (d) and (g) are typical large size STM topographic images of well cleaved terraces. Using the above K-means clustering method, the spatial distribution of principal responses and the corresponding principal responses of Ni-122, Co-122, and Cr-122 are presented in Fig. 3(b) and (c), Fig. 3(e) and (f) and Fig. 3(h) and (i), respectively. Note that, in addition to SC, in-gap and S-shape states, L-shape state are observed in all crystals. The L-shape states are presented as yellow curves in Fig. 3(c), (f) and (i). The dominant domains in Fig. 3(b), (e) and (h) are the percolated blue areas, which corresponds to the blue curves in Fig. 3(c), (f) and (i) as SC state in Ni-122 and Co-122, and metallic state in Cr-122, respectively, consistent with the bulk physical properties of the samples. All those samples share a substantial volume of green and yellow areas in the blue matrix, which correspond to the S-shape state (green curves) and L-shape state (yellow curves) in Fig. 3(c), (f) and (i). In Fig. 3(b) and (e), both superconducting Ni-122 and Co-122 surfaces have brown areas which correspond to the in-gap state (brown curves) in Fig. 3(c) and (f), while in Fig. 3(g) the in-gap state is not observed on the non-superconducting Cr-122 surface. Although the S-shape, L-shape and in-gap states are immersed in the SC (or metallic for Cr-122) matrix, the spatial distribution of those states is not correlated. Fig. 3(j) shows the statistics of the area percentages of each principal response in Ni-122, Co-122 and Cr-122. The volume of the majority domains (SC or metallic) are similar for the three sets, but the volumes of the S-shape and L-shape states show noticeably difference between the SC (Ni-122 and Co-122) and metallic (Cr-122) compounds. In Cr-122, the percentage of L-shape state has 2.4 times more than in Ni-122(Co-122), while S-shape state is rarely found. Although the relative percentage of S- or L- shape states are different, the total volume of the two states is quite similar in the three compounds in spite of that the Cr-122 is non-SC, Ni-122 is underdoped SC and Co-122 is optimal doped SC, coincident with

the same amount of hole ($\text{Cr}_{0.04}$) / electron ($\text{Ni}_{0.04}$ and $\text{Co}_{0.08}$) numbers doped into the three compounds. It is important to note that while the distribution of those states in Co-122 and Cr-122 is quite uniform, Ni-122 shows strong spatial variations. In Ni-122, there are phase segregated areas with almost pure SC state, and areas with highly mixed four electronic states.

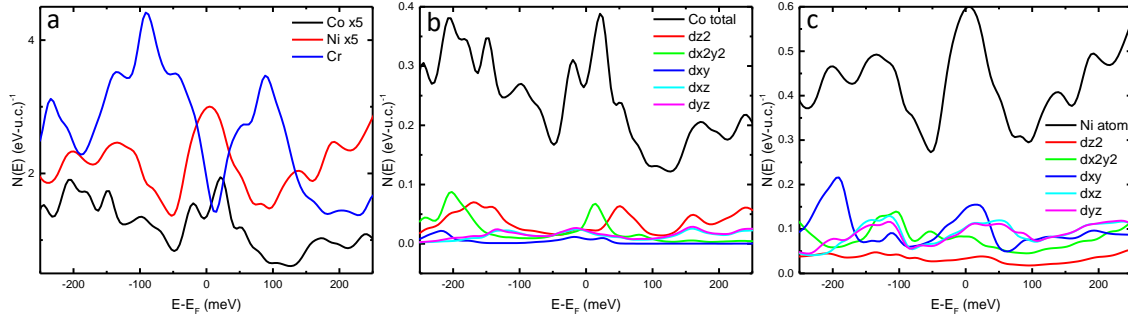


Fig. 4 | DFT calculation of 122 doped with Co, Ni and Cr. Panel (a) show the dopant atom total density-of-states for all 3 calculations; note that the values for Co and Ni have been multiplied by a factor of 5 to allow plotting on the same scale. Panels (b) and (c) depict dopant atom total and orbital-resolved densities-of-states for Co and Ni, respectively. Note the substantial similarity (apart from the vertical scale change) between the Co and Ni dopant atom total DOS in panels (b) and (c). Note the variation in vertical scales.

Fig. 3(k) shows a direct comparison of the average LDOS of the in-gap state in Ni-122 and Co-122. The in-gap state of Ni-122 samples shows a higher density of state around the Fermi level and asymmetrically suppressed superconducting coherent peaks. The different form of the in-gap states in two compounds and the fact that in our systematic experiments the zero-energy peak state is only observed in the Ni-122 and Co-122 crystals, never in Cr-122 strongly suggest that the robust in-gap state in iron-based 122 samples is originated from Co/Ni dopant, rather than Fe defects²⁵. Fig. 4 shows the result of DFT calculations of BaFe_2As_2 alloyed with Co, Ni and Cr: with one dopant atom (Co, Ni or Cr) substituted for Fe in a $2 \times 2 \times 1$ supercell of the orthorhombic low-temperature cell, or one dopant atom per 32 Fe atoms. This means that the dopant atoms are

far enough apart (over 1.1 nm) that they interact rather little, as is ideal for this calculation. Fig. 4(a) shows a comparison of the DOS near the Fermi level due to the dopant atoms. This approximates the LDOS in the immediate vicinity of this atom, which varies considerably, both in magnitude and in shape. Note that the Co and Ni curves are multiplied by 5 for ease of display, to focus on the shape. Both Co and Ni show some evidence of an “in-gap”, or near-Fermi level state (although the superconducting coherence peaks are of course absent here), while the Cr plot does not show this Fermi-level feature. It is interesting that the orbital-resolved origins of the in-gap state for Co and Ni are slightly different as shown in the orbital-resolved DOS calculations in Fig. 4(b) and (c), but that the total atomic DOS curves are remarkably similar. For Co dopant, the main contributors to the in-gap state are the e_g subset orbitals ($d_{x^2-y^2}$, d_{z^2}), but for Ni dopant, the t_{2g} subset orbitals (d_{xy} , d_{xz} , and d_{yz}) provide most of the DOS for the near-Fermi level feature. Previous results²⁸ found that Ni and Co doping affect T_c similarly in Ba-122 when considered as the number of charges added per Fe, suggesting that the local character of the dopant atom (i.e. Ni or Co) matters little for the superconductivity. The substantial similarity of the shape of the Co and Ni atomic DOS curves in Figures 4(b) and 4(c) supports this finding. It is sensible that the Ni atomic DOS is somewhat greater than that of Co, given the extra electron associated with Ni. The variation in orbital DOS does, however, suggest the importance of local character in the generation of these near-Fermi-level states. This is consistent with previous work on Cu-doped Ba-122²⁹ which shows only minor superconductivity despite a comparable charge count to the much more robust Ni and Co superconductors, and with theoretical suggestions³⁰ regarding the effects of charge dopants in these materials.

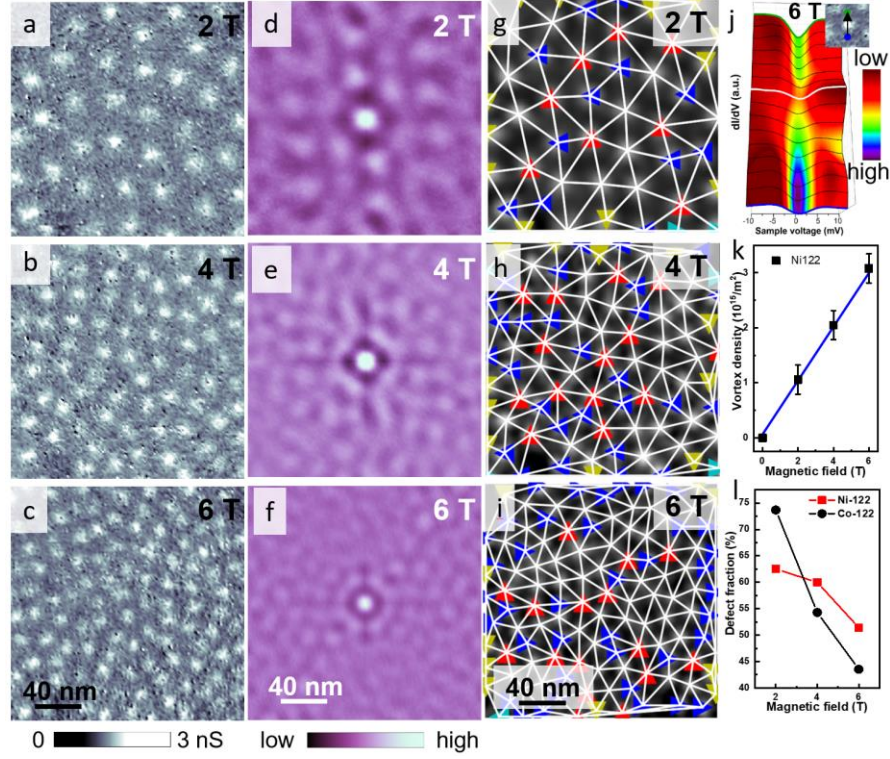


Fig. 5 | Vortex imaging in Ni-122 (a), (b) and (c) STS maps at E_F show the vortex lattices on the same location at various vertical magnetic field. ($V_{\text{Bias}} = -10$ mV, $I_t = 100$ pA and $T = 4.2$ K). (d), (e) and (f) Two-dimensional Self-correlation images calculated from vortex images shown in (a), (b) and (c). (g), (h) and (i) Delaunay triangulation diagrams overlaid on vortex images shown in (a), (b) and (c). Triangles emphasize the vortices with nearest neighbors different from 6 (cyan: 3; yellow: 4; blue: 5 and red: 7). (j) Spatial evolution of STS crossing a vortex core center along the black arrow in the inset. The spectra are offset for clarity. (k) Magnetic field dependent vortex density in Ni-122. (l) The fractions of defect-vortex at different magnetic fields for Ni-122 and Co-122.

To reveal the origin of various states, the samples were investigated under magnetic field applied perpendicular to the cleavage surfaces. The influence of magnetic field to SC state is well studied. Under magnetic field, the superconducting state transforms into the Abrikosov state by forming a vortex structure, where non-superconducting cores are surrounded by superconducting areas. Such a vortex structure can be imaged by spatial STS mapping around the Fermi level, with

higher local density of state bright spots in the cores³¹⁻³³. Shown in Fig. 5 (a), (b) and (c) are the STS maps at Fermi level (zero bias) under vertical magnetic field of 2, 4 and 6 T respectively, collected from the same location of a Ni-122 surface. STS curves cross a vortex core are plotted in Fig. 5(j) to demonstrate the spatial evolution of the tunneling conductance. Approaching to the core center, zero bias conductance increases, and superconducting coherence peaks are suppressed. Consistent with previous observations from electron-doped 122, no Andreev bound state is observed up to 6 T in the vortices of Ni-122³³⁻³⁴. The Ginzburg-Landau coherence lengths and the vortex lattice constants extracted from the normalized azimuthally averaged radial of average vortices in the STS maps and their self-correlation images are 4.8, 4.5, 4.1 nm and 33.7, 24.0, 19.5 nm at 2, 4 and 6 Tesla, respectively. The density of vortices increases linearly with the magnetic field as shown in Fig. 5(k). By fitting the applied magnetic field dependent vortex densities, magnetic flux is extracted as $\Phi = (1.96 \pm 0.4) \times 10^{-15} \text{ Tm}^2$, which is in good agreement with the single flux quantum of $\Phi_0 = 2.07 \times 10^{-15} \text{ Tm}^2$ ³¹⁻³³.

The symmetry of vortex lattices changes dramatically with the increase of the magnetic field. Fig. 5(d), (e) and (f) show two-dimensional autocorrelation images calculated from vortex images in (a), (b) and (c). The vortex forms a weak triangular lattice at 2 T as six-folded correlation is shown in Fig. 5(d). At higher fields, the vortex lattice gradually changes to a rectangular shape at 4 T (Fig. 5(e)) and becomes more isotropic ring-like structure at 6 T (Fig. 5(f)). The emergence of 4-fold symmetry on top of 6-fold symmetry suggests that the configuration of the vortices is affected by the underlying crystal lattice. The result also suggests that the distance correlation among the vortices is stronger than the orientational correlation in Ni-122. The Delaunay triangulation analysis are shown in Fig. 5(g), (h) and (i). The defect vortices are symbolized by blue and red triangles, which have 5 and 7 nearest neighbors rather than 6 in regular vortex lattice.

It is interesting to point out that although the vortex densities for the two compounds are almost the same, the vortex matter for Ni-122 and Co-122 is different. In contrast to the gradual change of the vortex lattice in Ni-122, the vortex lattice does not change too much in Co-122 under magnetic field up to 6 T. The difference is also reflected in the different trends of defect-vertex fractions of the two compounds, shown in Fig. 5(i) and Fig. S1 in supplementary info. While the vortex matter of Ni-122 is quite similar to LiFeAs³², its behavior in Co-122 is more close to (BaK)Fe₂As₂³⁴. We anticipate the different vortex matters for Ni-122 and Co-122 should relate to the drastic different phase distributions in the two compounds: uniformly scattered S, L and in-gap states in the Co-122 compound serve as pinning nuclei for stabilizing the hexagonal vortex lattice, consistent with the observation of surface pinning effect in (BaK)Fe₂As₂ sample³⁴. This observation suggests the role of the inhomogeneous electronic states plays an important role in the higher upper critical fields in the FeSC.

The magnetic field influence on all states is summarized in Fig. 6, which shows the result from Co-122 with field up to 6 Tesla, each set of field dependent spectra are extracted from the same atomic locations. The gradually increased zero bias conductance and suppressed superconducting coherent peaks under magnetic field shown in Fig. 6(a) has been discussed in the last few paragraphs. For the in-gap state, the peak is pinned at the Fermi level even up to 6 Tesla, but the intensity of the peak increases slightly with the magnetic field as shown in Fig. 6(b). A similar robust zero-energy bound state was also observed on Fe(Te,Se)³⁵ which is caused by interstitial Fe impurities.

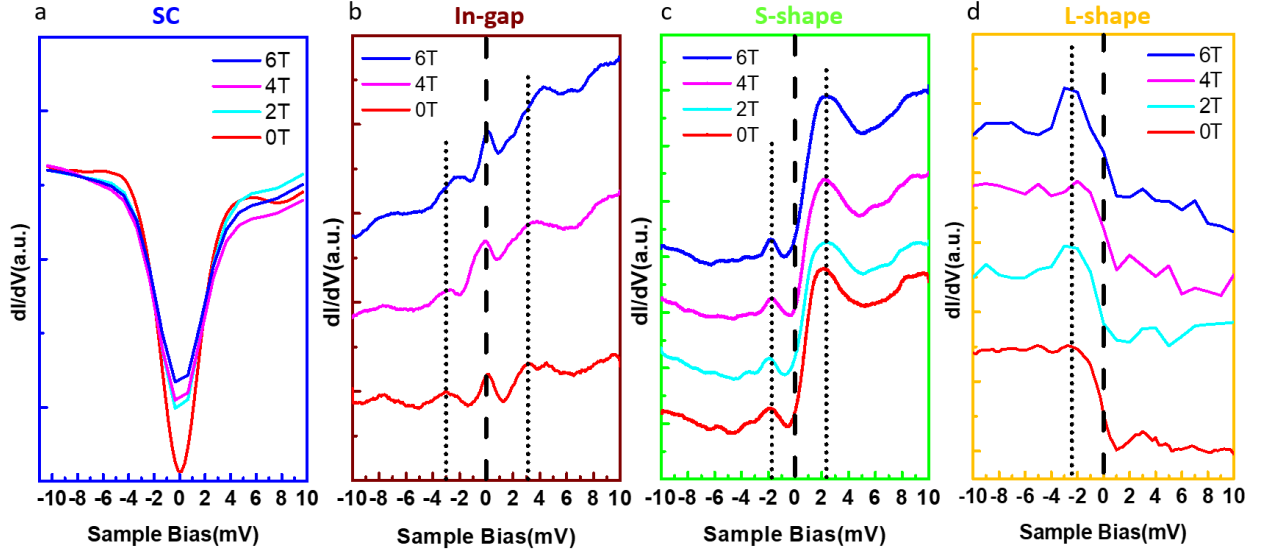


Fig. 6 | Magnetic field dependence of the spectra of Co-122. (a), (b), (c) and (d) SC, in-gap, S-shape and L-shape spectra measured in magnetic field of 0 - 6 Tesla at 2.0 K. The dash lines are guides for the eye. Each set of field dependent spectra are collected at the same atomic locations, curves in (b), (c) and (d) are offset vertically for clarity.

For both the S-shape and L-shape states, there is no significant change detected up to 6 T as shown in Fig. 6(c) and (d). These observations exclude Kondo effect of magnetic moment in metal/superconductor since no splitting was found in magnetic field dependence spectra. Although the S-shape and L-shape spectra look similar to the Fe-vacancy-induced bound state found in K-doped iron selenide³⁶, their extremely weak field dependent indicates that either the g-factor in our case is far smaller than 2.1 or they are from a different origin.

The L shape like state has been identified as spin density wave spectrum with signature features of highly asymmetric with respect to Fermi level and large residual DOS at E_F ^{20,23}, which is found coexisting and competing with SC states in under- and over-doped $\text{NaFe}_{1-x}\text{Co}_x\text{As}$ (Co-111) FeSC. In our current comparison experiment of 122 system, we further found that 1) the SDW spectrum exists in both electron and hole doped 122 compounds; 2) the SDW survives even in the

optimal doped Co-122 crystals, although the volume is very small (2.3%); 3) the highly asymmetric spectrum resulted from the particle-hole symmetry is tilted towards positive bias, similar to the positive bias in Co-111 case. The results suggest that the similar coexistent of local moments and itinerant electrons model^{20,23} should also hold for the 122 system, with the physical picture of cooper pairing can occur when portions of the Fermi surface are already gapped by the SDW order. The much lower percentage of L shape state in Cr-122 might hint as to why there is no SC in the Cr-122.

The S shape state was not reported previously, although the present data set cannot firmly prove the origin of the phase, we anticipate it is another form of magnetic state, based on its spectral features. The main differences between the S and L shape states are: 1) the asymmetric spectrum is tilted to the negative bias; 2) the Fermi surface residual of the L shape is low, very close to the bottom of SC gap, but for S shape the Fermi surface residual is much higher (Fig. 3 (c) (f) and (i)); 3) the volume percentage of the S state is lowest in non-SC Cr-122, and highest in optimum doped Co-122. Notably, from the volumes of the S state of the three compounds, the behavior of the S shape state is more cooperative with the superconducting state, rather than competitive with SC as observed for the L shape state. This abnormal behavior and the highly elevated LDOS at Fermi level suggest the S-shape state should have the same origin as the muon spin rotation observation of a different component of spin density wave order in Co-122²¹⁻²² and the neutron study of the identification of a short-range spin-glass state in Ni-122¹². In the muon spin rotation study, a spatially inhomogeneous magnetic state develops below T_c and it has a constructive rather than a competitive relationship with SC near optimal or even overdoped Co-122 samples²¹⁻²². A follow-up theoretical study explains the distinct magnetic phases using an impurity-induced order which is stabilized by a multiple-Co dopant effect³⁷. Future spin-polarized STM studies are essential to

further confirm and identify the relation between the S, L shape states as well as the in-gap state with the superconductivity phase.

Conclusion

In summary, $\text{Ba}(\text{Fe}_{1-x}\text{T}_x)_2\text{As}_2$ single crystals in three different phases, optimal doped SC Co-122, coexisting SC and AFM Ni-122, and non-SC Cr-122, are studied at atomic surface levels using STM/S. All these single crystals show various nanometer-size local electronic inhomogeneities which are not related to the surface topography. The total volume of the inhomogeneous areas is similar in the three compounds, coincident with the same amount of electron ($\text{Ni}_{0.04}$ and $\text{Co}_{0.08}$) / hole ($\text{Cr}_{0.04}$) numbers doped into the three crystals. But the distribution of the inhomogeneous electronic states is different; they are uniformly distributed all around the sample in nanometer-size clusters in optimal-doped Co-122 crystals, but more segregated in underdoped Ni-122 samples. Using a K-means clustering statistic method, the local electronic states are categorized as S-shape, L-shape and in-gap states immersed in the matrix of SC state for Ni-122 and Co-122, S-shape and L-shape states in metallic phase for Cr-122. The spatial distribution of S-shape, L-shape and in-gap states are not correlated. The comparison of vortex structures from an external magnetic field in areas with pure SC state or mixed inhomogeneous area indicates that the S-shape, L-shape and in-gap states serve as pinning nuclei for stabilizing the hexagonal vortex lattice. By combining all the observations including the volume fractions of the three states, LDOS, field dependent behavior and global properties in three sets of samples, we confirm the in-gap state in SC crystals originates from magnetic Co/Ni dopants, identify the origin of the L-shape state is from the spin density wave which competes with the SC phase, and find the existence of another form of magnetic order as S-shape state which constructively cooperates with the SC phase or serves as an essential element for SC.

Method

Single crystals of $\text{Ba}(\text{Fe}_{0.92}\text{Co}_{0.08})_2\text{As}_2$, $\text{Ba}(\text{Fe}_{0.96}\text{Ni}_{0.04})_2\text{As}_2$ and $\text{Ba}(\text{Fe}_{0.96}\text{Cr}_{0.04})_2\text{As}_2$ were grown out of self-flux from FeAs and Co (or Ni, Cr)As binaries, a synthesis method similar to our previous reports ²⁴. Phase purity, crystallinity, and the atomic occupancy of all crystals were checked by collecting Powder X-ray diffraction (XRD) data on an X'Pert PRO MPD diffractometer (Cu $K_{\alpha 1}$ radiation, $\lambda=1.540598$ Å); The average chemical composition of each crystal was measured with a Hitachi S3400 scanning electron microscope operating at 20 kV, and use of energy-dispersive x-ray spectroscopy (EDS).

All crystals were cleaved in ultra-high vacuum (UHV) at ~ 78 K and then immediately transferred to the Scanning Tunneling Microscopy/Spectroscopy (STM/S) head which was precooled to 4.2 K without breaking the vacuum. The STM/S experiments were carried out at 2.0 K or 4.2 K using a UHV low-temperature and high field scanning tunneling microscope with base pressure better than 2×10^{-10} Torr ²⁵. Pt-Ir tips were mechanically cut then conditioned on clean Au (111) and checked using the topography, surface state and work function of Au (111) before each measurement. The STM/S were controlled by a SPECS Nanonis control system. Topographic images were acquired in constant current mode with bias voltage applied to sample, and tip grounded. All the spectroscopies were obtained using the lock-in technique with a modulation of 0.1 to 1 mV at 973 Hz on bias voltage, dI/dV . Line spectroscopies and Current-Imaging-Tunneling-Spectroscopy were collected over a grid of pixels at bias ranges around Fermi level using the same lock-in amplifier parameters. During STM/S measurement, a magnetic field up to 9 Tesla was applied perpendicular to the crystal surfaces.

The K-means clustering analysis was performed in PYTHON language using PYCROSCOPY package ²⁶. The analysis uses an unsupervised learning algorithm, with the goal to find groups in the data, with the number of groups represented by the variable K . All STS datasets were studied using the same code.

Acknowledgments

This research was conducted at the Center for Nanophase Materials Sciences, which is a DOE Office of Science User Facility. L.L., A.S., D.S.P. and Z.G.'s research are supported by the U.S. DOE, Office of Science, Basic Energy Sciences, Materials Science and Engineering Division.

Author contributions

Q.Z., M.F, Z.W. and Z.G. conducted the STM/S studies and data analysis; L.L. and A.S. grew the crystals; D.P. did the DFT calculations; all authors contributed to the discussion and writing of the manuscript.

Supporting information

Reference

1. Lee, P. A.; Nagaosa, N.; Wen, X.-G., Doping a Mott insulator: Physics of high-temperature superconductivity. *Reviews of Modern Physics* **2006**, *78* (1), 17-85.
2. Dai, P., Antiferromagnetic order and spin dynamics in iron-based superconductors. *Reviews of Modern Physics* **2015**, *87* (3), 855-896.
3. Hashimoto, M.; Vishik, I. M.; He, R.-H.; Devereaux, T. P.; Shen, Z.-X., Energy gaps in high-transition-temperature cuprate superconductors. *Nature Physics* **2014**, *10*, 483.
4. Scalapino, D. J., A common thread: The pairing interaction for unconventional superconductors. *Reviews of Modern Physics* **2012**, *84* (4), 1383-1417.
5. Tsuei, C. C.; Kirtley, J. R., Pairing symmetry in cuprate superconductors. *Reviews of Modern Physics* **2000**, *72* (4), 969-1016.
6. Wang, F.; Lee, D.-H., The Electron-Pairing Mechanism of Iron-Based Superconductors. *Science* **2011**, *332* (6026), 200.

7. Chubukov, A., Pairing Mechanism in Fe-Based Superconductors. *Annual Review of Condensed Matter Physics* **2012**, *3* (1), 57-92.
8. Bang, Y.; Stewart, G. R., Anomalous Scaling Relations and Pairing Mechanism of the Fe-based Superconductors. *Journal of Physics: Conference Series* **2017**, *807*, 052003.
9. Huang, D.; Hoffman, J. E., Monolayer FeSe on SrTiO₃. *Annual Review of Condensed Matter Physics* **2017**, *8* (1), 311-336.
10. Rotter, M.; Tegel, M.; Johrendt, D., Superconductivity at 38 K in the iron arsenide (Ba_{1-x}K_x)Fe₂As₂. *Phys Rev Lett* **2008**, *101* (10), 107006.
11. Sefat, A. S.; Singh, D. J.; Jin, R. Y.; McGuire, M. A.; Sales, B. C.; Ronning, F.; Mandrus, D., Ba₂As₂ single crystals (T = Fe, Co, Ni) and superconductivity upon Co-doping. *Physica C* **2009**, *469* (9-12), 350-354.
12. Lu, X. Y.; Tam, D. W.; Zhang, C. L.; Luo, H. Q.; Wang, M.; Zhang, R.; Harriger, L. W.; Keller, T.; Keimer, B.; Regnault, L. P.; Maier, T. A.; Dai, P. C., Short-range cluster spin glass near optimal superconductivity in BaFe_{2-x}Ni_xAs₂. *Phys Rev B* **2014**, *90* (2), 024509.
13. Jiang, S.; Xing, H.; Xuan, G. F.; Wang, C.; Ren, Z.; Feng, C. M.; Dai, J. H.; Xu, Z. A.; Cao, G. H., Superconductivity up to 30 K in the vicinity of the quantum critical point in BaFe₂(As_{1-x}P_x)₂. *J Phys-Condens Mat* **2009**, *21* (38), 382203.
14. Sefat, A. S.; Singh, D. J.; VanBebber, L. H.; Mozharivskiy, Y.; McGuire, M. A.; Jin, R. Y.; Sales, B. C.; Keppens, V.; Mandrus, D., Absence of superconductivity in hole-doped BaFe_{2-x}Cr_xAs₂ single crystals. *Phys Rev B* **2009**, *79* (22), 224524.
15. Pratt, D. K.; Kim, M. G.; Kreyssig, A.; Lee, Y. B.; Tucker, G. S.; Thaler, A.; Tian, W.; Zarestky, J. L.; Bud'ko, S. L.; Canfield, P. C.; Harmon, B. N.; Goldman, A. I.; McQueeney, R. J., Incommensurate Spin-Density Wave Order in Electron-Doped BaFe₂As₂ Superconductors. *Phys Rev Lett* **2011**, *106* (25), 257001.
16. Wang, F.; Zhai, H.; Ran, Y.; Vishwanath, A.; Lee, D. H., Functional Renormalization-Group Study of the Pairing Symmetry and Pairing Mechanism of the FeAs-Based High-Temperature Superconductor. *Phys Rev Lett* **2009**, *102* (4), 047005.
17. Si, Q. M.; Abrahams, E., Strong correlations and magnetic frustration in the high T_c iron pnictides. *Phys Rev Lett* **2008**, *101* (7), 076401.
18. Kou, S. P.; Li, T.; Weng, Z. Y., Coexistence of itinerant electrons and local moments in iron-based superconductors. *Epl-Europhys Lett* **2009**, *88* (1), 17010.
19. You, Y. Z.; Yang, F.; Kou, S. P.; Weng, Z. Y., Magnetic and superconducting instabilities in a hybrid model of itinerant/localized electrons for iron pnictides. *Phys Rev B* **2011**, *84* (5), 054527.
20. Zhou, X. D.; Cai, P.; Wang, A. F.; Ruan, W.; Ye, C.; Chen, X. H.; You, Y. Z.; Weng, Z. Y.; Wang, Y. Y., Evolution from Unconventional Spin Density Wave to Superconductivity and a Pseudogaplike Phase in NaFe_{1-x}CoxAs. *Phys Rev Lett* **2012**, *109* (3), 037002.
21. Bernhard, C.; Wang, C. N.; Nuccio, L.; Schulz, L.; Zaharko, O.; Larsen, J.; Aristizabal, C.; Willis, M.; Drew, A. J.; Varma, G. D.; Wolf, T.; Niedermayer, C., Muon spin rotation study of magnetism and superconductivity in Ba(Fe_{1-x}Cox)₂As₂ single crystals. *Phys Rev B* **2012**, *86* (18), 184509.
22. Bernhard, C.; Drew, A. J.; Schulz, L.; Malik, V. K.; Rossle, M.; Niedermayer, C.; Wolf, T.; Varma, G. D.; Mu, G.; Wen, H. H.; Liu, H.; Wu, G.; Chen, X. H., Muon spin rotation study of magnetism and superconductivity in BaFe_{2-x}CoxAs₂ and Pr_{1-x}Sr_xFeAsO. *New J Phys* **2009**, *11*, 055050.
23. Cai, P.; Zhou, X. D.; Ruan, W.; Wang, A. F.; Chen, X. H.; Lee, D. H.; Wang, Y. Y., Visualizing the microscopic coexistence of spin density wave and superconductivity in underdoped NaFe_{1-x}CoxAs. *Nat Commun* **2013**, *4*, 1596.
24. Sefat, A. S., Bulk synthesis of iron-based superconductors. *Curr Opin Solid St M* **2013**, *17* (2), 59-64.
25. Zou, Q.; Wu, Z. M.; Fu, M. M.; Zhang, C. M.; Rajput, S.; Wu, Y. P.; Li, L.; Parker, D. S.; Kang, J.; Sefat, A. S.; Gai, Z., Effect of Surface Morphology and Magnetic Impurities on the Electronic Structure in Cobalt-Doped BaFe₂As₂ Superconductors. *Nano Lett* **2017**, *17* (3), 1642-1647.

26. Somnath, S.; Smith, C. R.; Jesse, S.; Laanait, N., Pycroscopy - An Open Source Approach to Microscopy and Microanalysis in the Age of Big Data and Open Science. *Microscopy and Microanalysis* **2017**, *23* (S1), 224-225.
27. Hoffman, J. E., Spectroscopic scanning tunneling microscopy insights into Fe-based superconductors. *Rep Prog Phys* **2011**, *74* (12), 124513.
28. Canfield, P. C.; Bud'ko, S. L.; Ni, N.; Yan, J. Q.; Kracher, A., Decoupling of the superconducting and magnetic/structural phase transitions in electron-doped BaFe₂As₂. *Phys Rev B* **2009**, *80* (6), 060501(R).
29. Ni, N.; Thaler, A.; Yan, J. Q.; Kracher, A.; Colombier, E.; Bud'ko, S. L.; Canfield, P. C.; Hannahs, S. T., Temperature versus doping phase diagrams for Ba(Fe_{1-x}TM_x)₂As₂ (TM=Ni,Cu,Cu/Co) single crystals. *Phys Rev B* **2010**, *82* (2), 024519.
30. Berlijn, T.; Lin, C. H.; Garber, W.; Ku, W., Do Transition-Metal Substitutions Dope Carriers in Iron-Based Superconductors? *Phys Rev Lett* **2012**, *108* (20), 207003.
31. Pan, S. H.; Hudson, E. W.; Gupta, A. K.; Ng, K. W.; Eisaki, H.; Uchida, S.; Davis, J. C., STM studies of the electronic structure of vortex cores in Bi₂Sr₂CaCu₂O_{8+δ}. *Phys Rev Lett* **2000**, *85* (7), 1536-1539.
32. Hanaguri, T.; Kitagawa, K.; Matsubayashi, K.; Mazaki, Y.; Uwatoko, Y.; Takagi, H., Scanning tunneling microscopy/spectroscopy of vortices in LiFeAs. *Phys Rev B* **2012**, *85* (21), 214505.
33. Yin, Y.; Zech, M.; Williams, T. L.; Wang, X. F.; Wu, G.; Chen, X. H.; Hoffman, J. E., Scanning tunneling spectroscopy and vortex imaging in the iron pnictide superconductor BaFe_{1.8}Co_{0.2}As₂. *Phys Rev Lett* **2009**, *102* (9), 097002.
34. Shan, L.; Wang, Y. L.; Shen, B.; Zeng, B.; Huang, Y.; Li, A.; Wang, D.; Yang, H. A.; Ren, C.; Wang, Q. H.; Pan, S. H. H.; Wen, H. H., Observation of ordered vortices with Andreev bound states in Ba_{0.6}K_{0.4}Fe₂As₂. *Nature Physics* **2011**, *7* (4), 325-331.
35. Yin, J.; Wu, Z.; Wang, J.; Ye, Z.; Gong, J.; Hou, X.; Shan, L.; Li, A.; Liang, X.; Wu, X., Observation of a robust zero-energy bound state in iron-based superconductor Fe(Te, Se). *Nature Physics* **2015**, *11* (7), 543.
36. Li, W.; Ding, H.; Deng, P.; Chang, K.; Song, C.; He, K.; Wang, L.; Ma, X.; Hu, J.-P.; Chen, X., Phase separation and magnetic order in K-doped iron selenide superconductor. *Nature Physics* **2012**, *8* (2), 126.
37. Gastiasoro, M. N.; Hirschfeld, P. J.; Andersen, B. M., Impurity states and cooperative magnetic order in Fe-based superconductors. *Phys Rev B* **2013**, *88* (22), 220509(R).